



# Combining heterogeneous photocatalysis and enzymatic catalysis via membrane: Conversion of biomass for H<sub>2</sub> production from water

Zhaoyi Li, Zhen Sun, Guan Zhang<sup>\*</sup>

State Key Laboratory of Urban Water Resource and Environment, Shenzhen Key Laboratory of Organic Pollution Prevention and Control, School of Civil and Environmental Engineering, Harbin Institute of Technology, Shenzhen, Shenzhen 518055, PR China

## ARTICLE INFO

### Keywords:

Biomass conversion  
Hydrogen production  
Enzymatic hydrolysis  
Photocatalysis  
Cu/Ni deposited Titania

## ABSTRACT

Solar reforming cellulosic biomass into hydrogen is an attractive research topic for sustainable biomass waste utilization and renewable energy development. To exert the advantages of enzymatic catalysis and heterogeneous photocatalysis, a glass fiber membrane integrated process that combines enzymatic hydrolysis of cellulose with sacrificial photocatalytic H<sub>2</sub> production from water under mild condition has been proposed as an example of integrating enzymatic catalysis and heterogeneous photocatalysis. Specifically, a low-cost Cu<sub>0.5</sub>Ni<sub>0.5</sub>-TiO<sub>2</sub> photocatalyst has been developed with presenting remarkable H<sub>2</sub> production performance even comparable with Pt-TiO<sub>2</sub> under UV light irradiation. The synergistic effect of Cu and Ni co-deposition onto TiO<sub>2</sub> has been found to improve the photocatalytic H<sub>2</sub> production. The condition for enzymatic hydrolysis of cellulose to generate glucose has been optimized in terms of reaction temperature, solution pH, types of cellulase and inorganic ions in order to obtain higher yields of glucose. To integrate the enzymatic catalysis and photocatalysis together, the glass fiber membrane with superior glucose penetration capability has been screened out. Lastly, the coupling of photocatalytic H<sub>2</sub> production from water based on the Cu<sub>0.5</sub>Ni<sub>0.5</sub>-TiO<sub>2</sub> photocatalyst and enzymatic hydrolysis of cellulose has been quantitatively evaluated in both mixed and membrane-separation systems. The membrane-separation system can avoid the depletion of cellulase activity induced by photocatalytic oxidation, and thus presents higher H<sub>2</sub> production efficiencies with apparent quantum efficiency of 3.07 % at 365 ± 10 nm irradiation in initial 5 h. This work demonstrates that inorganic membrane integrated enzymatic catalysis and photocatalysis can be a powerful tool for different potential applications.

## 1. Introduction

Natural enzyme catalytic reactions exhibit high selectivity and yields that usually achieved at ambient condition, which has been widely utilized in fields of biochemical synthesis and conversion [1–3]. For instance, solid cellulosic biomass materials with rigid structure can be efficiently depolymerized into glucose by enzyme at mild condition (e.g. pH 4–7, reaction temperature 300–320 K) [4–6], comparing with the chemical depolymerization of cellulose that is normally performed at harsh reaction conditions (e.g. strong acidic or alkaline environment) [7–9]. To exert the advantages of these biological systems with the reactivity of artificial heterogeneous photocatalysts, researchers have devised sequential and concurrent reactions that combine enzymes and photocatalysts [10–12]. However, concurrent reactions are difficult to proceed since photocatalyst and enzymatic catalyst generally operate in different media at different temperatures and can deactivate each other.

Particularly, the photocatalyst can produce a series of reactive oxidants such as •OH, H<sub>2</sub>O<sub>2</sub>, O<sub>2</sub><sup>•−</sup>, <sup>1</sup>O<sub>2</sub>, holes, etc., which can destroy the enzyme and inhibit the enzymatic activity [11]. Hence, it is necessary to develop a system that can efficiently integrate the two powerful catalytic processes.

H<sub>2</sub> as an energy carrier will perform more roles in renewable energy development in future, and sunlight driven semiconductor photocatalytic water splitting for H<sub>2</sub> production is considered as one of the green and promising H<sub>2</sub> production technologies [13–15]. Although photocatalytic H<sub>2</sub> production from water without sacrificial donors or coupling with water oxidation cocatalyst to generate O<sub>2</sub> simultaneously have been investigated for few decades, and make significant breakthroughs recently [16–18], the efficiency of overall water splitting is still lower than the sacrificial H<sub>2</sub> production system [19,20]. However, the problem of the sacrificial H<sub>2</sub> production is that it normally relies on valuable and expensive sacrificial agents such as alcohols, sugars,

<sup>\*</sup> Corresponding author.

E-mail address: [zhangguan@hit.edu.cn](mailto:zhangguan@hit.edu.cn) (G. Zhang).

<https://doi.org/10.1016/j.apcatb.2023.123069>

Received 26 March 2023; Received in revised form 16 May 2023; Accepted 2 July 2023

Available online 8 July 2023

0926-3373/© 2023 Elsevier B.V. All rights reserved.

amines, etc, which is not reliable to practical application due to the economic consideration [21,22]. The utilization of biomass waste or its derivatives as the sacrificial agents is therefore an attractive proposition [23–25]. A typical semiconductor for photocatalytic  $H_2$  production is the stable and abundant  $TiO_2$  deposited with Pt cocatalyst [26,27]. However, noble metal based  $H_2$  evolution cocatalyst is also not affordable for large scale application, the low cost transition metal (Cu, Ni, Co, Mo, etc.) based co-catalysts etc. have been reported as potential substitutes [28,29]. Particularly, the bimetallic metals Cu and Ni commodified  $TiO_2$  photocatalyst displays a superior higher activity compared to monometallic counterparts [30–32]. The physiochemical parameters of deposited Cu and Ni based co-catalysts such as composition (metal, oxide or hydroxide form), morphology (nanoparticle, nanodot or nanowire), oxidation states (0, +1, +2), crystallinity (crystalline or amorphous) and structure (core-shell), etc., depending on its preparation and synthesis process, can significantly influence the  $H_2$  evolution activity, and thus further investigating the role of Cu and Ni based co-catalysts in  $H_2$  evolution is highly in demand.

In this work, we combined the two individual processes of enzyme catalytic cellulose depolymerization and photocatalytic  $H_2$  production through a membrane that allows depolymerized soluble products such as glucose can permeate from the enzymatic reaction module to photocatalytic reaction module. This physical separation avoids the damage of enzyme by reactive oxidants generated by photocatalysis. The permeable soluble organic contents can be utilized as sacrificial agents to enhance the water splitting reaction. Such an integration system can efficiently utilize biomass waste to produce renewable  $H_2$  fuel. To achieve this purpose, different ratios of Cu and Ni nanoparticles co-deposited  $TiO_2$  photocatalysts were prepared and characterized in order to find out the ideal composition of Cu and Ni co-catalyst for  $H_2$  evolution. Then, the cellulose depolymerization process was also optimized by investigating the roles of cellulase, metal ion, pH and temperature. Particularly, the promotion or inhibition effects of co-existing ions on the enzymatic activity was investigated. Finally, we integrated the two catalytic processes together through the membrane with superior glucose permeation capacity, to realize the simultaneous biomass conversion and  $H_2$  production. Arising from the particular effects of membrane in transferring glucose and blocking oxidative species, the membrane-separation system exhibited higher  $H_2$  production performance in long-term reaction compared with the all-in-one mixed system.

## 2. Experimental

### 2.1. Materials and reagents

Cellulase from *Aspergillus niger* (carrier for dextrin, purchased from Aladdin), Cellulase from *Aspergillus niger* (carrier for starch, purchased from Aladdin), Cellulase (*Trichoderma Viride*, purchased from Scientific Phygene), Cellulase (*Trichoderma Viride*, Food Grade, purchased from LongKete), Cellulase (*Trichoderma Reesei*, purchased from Aladdin). All metal salts, ethanol, cellulose, glucose and other chemical reagents were purchased from Aladdin Co., Ltd. P25  $TiO_2$  was purchased from Evonik Industries AG.

### 2.2. Sample preparation

Cu, Ni and Pt deposited  $TiO_2$  samples were carried out with simple  $NaBH_4$  reduction method [9]. Typically, 1.0 g/L P25  $TiO_2$  was well dispersed into  $Ni(NO_3)_2$ ,  $Cu(NO_3)_2$  and/or  $H_2PtCl_6$  solution with 1.0 wt % Cu or Ni against  $TiO_2$  and 3.0 wt% Pt against  $TiO_2$  to keep same molar ratio of metal deposition. Under vigorous stirring, 50 mL 0.53 M  $NaBH_4$  and 0.5 M NaOH mixed solution were slowly dropped into the  $TiO_2$  suspension. After 30 min stirring and reduction, the  $TiO_2$  suspension was filtrated and rinsed with DI water. The obtained powder was dried at 60 °C in an oven overnight for further use. Accordingly, different ratios

of Cu and Ni deposited  $TiO_2$  samples (denoted as  $Cu_xNi_{1-x}-TiO_2$ ,  $x = 0, 0.2, 0.5, 0.8$  and  $1.0$ ) were prepared by this way.

### 2.3. Sample characterization

The X-ray diffraction (XRD) patterns were obtained on an X-ray diffractometer (Bruker D8 Advance 250) from 10 to 80° with scan rate of 10 °/min. High resolution transmission electron microscope (HR-TEM) image was obtained on FEI-TALOS-F200X transmission electron microscope for the representative  $Cu_{0.5}Ni_{0.5}-TiO_2$  sample. ICP-OES (AGILENT 725-ES) was used to measure the practical contents of deposited metals on  $TiO_2$  samples. Agilent UV spectrophotometer (Cary-300) was used to analyze the photochemical behavior of samples in the light range from 200 to 800 nm. Photoluminescence (PL) spectra of the samples were obtained on a fluorescence spectrophotometer (Hitachi, F-4600) with excitation wavelength of 320 nm. Raman spectrometer (Thermo Fischer DXR) was used to characterize the surface chemical bond information of the sample under the condition of an excitation wavelength of 532 nm. X-ray photoelectron spectroscopy (XPS) measurements were performed on a PHI 5000 Versaprobe II electron spectrometer.

### 2.4. Enzymatic hydrolysis and analysis

Typically, 0.004 g of cellulase and 0.1 g of cellulose were added to 50 mL of deionized water (pH = 5.5), then placed in a magnetic stirring water bath at 45 °C for 48 h. Glucose was analyzed using DNS derivative approach [33,34]. The DNS agent was prepared by mixing 6.3 g 3, 5-dinitrosalicylic acid, 182 g potassium and sodium tartrate, 5.0 g phenol, 5.0 g sodium sulfite  $Na_2SO_3$  and 262 mL 2 M sodium hydroxide in 500 mL hot water. After the homogeneous solution was formed, the hot solution was cooled down to room temperature and diluted with water to a total volume of 1000 mL. Glucose reacts with DNS agent to produce brown color product, which can be monitored by UV-visible spectrometer at wavelength of 540 nm.

### 2.5. Photocatalytic hydrogen production

Photocatalytic hydrogen production experiment was carried out with all glass automatic on-line trace gas analysis system (Beijing Perfectlight Labsolar 6 A) connected with gas chromatograph (Agilent 7890B). A Xeon lamp (PLS-SXE300D from Beijing Perfectlight) was used as the UV light source. The photocatalytic  $H_2$  production experiments were carried out with two conditions. In the all-in-one mixed system, typically 100 mg cellulose, 4 mg cellulase, 0.03 M  $K^+$  and 50 mg  $Cu_{0.5}Ni_{0.5}-TiO_2$  photocatalyst were put in the reactor. The initial pH of suspension was 5.5 and light intensity was 1000 mW/cm<sup>2</sup>. After removal of air in the reactor, the xenon lamp ( $\geq 320$  nm) was turned on. The accumulated  $H_2$  in the reactor was quantified by online gas chromatograph. In the membrane-separation system, a home-made reactor with membrane interconnecting of enzymatic module and photocatalytic module was developed. The same quantities of cellulose, cellulase and potassium salt were added into the inner enzymatic module, while the photocatalyst was put into the outer photocatalytic module. The temperature of suspension was about 40 °C during photo illumination. In addition to cellulose used as model biomass material, different raw biomass substances including, bamboo powder, soybean straw powder, corn straw powder, peanut shell powder and wheat straw powder were also used for  $H_2$  production. The quantum efficiency for light to  $H_2$  conversion was measured using a 365 ± 10 nm band-pass filter. The hydroxyl radical concentration was measured by an indirect fluorescence spectrometry method using terephthalic acid (0.1 mM) as a probe, which gives an emission peak centered at 425 nm [35].

### 3. Results and discussion

#### 3.1. Synthesis and characterization of the photocatalyst

The Cu, Ni, and Pt deposited  $\text{TiO}_2$ (P25) and co-deposited  $\text{TiO}_2$  with different Cu/Ni ratios were prepared by simple aqueous  $\text{NaBH}_4$  reduction method. During the metal reduction process, the same molar ratio of Cu, Ni and Pt precursors were added into the  $\text{TiO}_2$  suspension. The practical mass of different metals deposited on  $\text{TiO}_2$  measured by ICP-OES shown in Table S1 slightly varied with the theoretical values. For Cu- $\text{TiO}_2$  and Ni- $\text{TiO}_2$  samples, the practical contents measured by ICP-OES are about 0.95 wt% vs  $\text{TiO}_2$ , which are lower than the theoretical value (1.0 wt%), indicating that a number of Cu and Ni ions were not reduced by  $\text{NaBH}_4$ . This could be induced by the fast adding  $\text{NaBH}_4$  solution during the reduction process. In contrast, the practical amount of Pt deposited on  $\text{TiO}_2$  is consistent with the theoretical value (3.0 wt %), implying nearly all the Pt metal ions were reduced. Interestingly, the practical mass and ratios of Cu/Ni on the mixed metals deposited samples are basically consistent with their theoretical values, implying all

the Cu and Ni metal ions were reduced. The ICP-OES analysis results confirmed that the Cu and Ni metals can be easily deposited on  $\text{TiO}_2$  by  $\text{NaBH}_4$  reduction. HR-TEM images of the representative mixed metal deposited  $\text{TiO}_2$  sample ( $\text{Cu}_{0.5}/\text{Ni}_{0.5}$ - $\text{TiO}_2$ ) clearly show the spherical Cu and Ni nanoparticles (dark spots) were deposited onto the larger  $\text{TiO}_2$  particles as shown in Fig. 1a. The particle sizes of deposited metals were measured about 1.5–3.0 nm according to the HR-TEM image. HADDF image and EDS mapping images (Fig. 1b–f) indicate the uniform distribution of Cu and Ni elements on the aggregated  $\text{TiO}_2$  particles, while there was no clear boundary of Cu and Ni nanoparticles.

XPS spectra shown in Fig. 2a–c reflect the change of surface chemical states of Ti, Cu and Ni in different samples. The Ti  $2p_{3/2}$  peaks (e.g. 458.5 eV) of Pt- $\text{TiO}_2$ , Cu- $\text{TiO}_2$  and Ni- $\text{TiO}_2$  samples clearly shift to relative lower binding energies compared to that of pure P25 sample, indicating that  $\text{Ti}^{3+}$  exists in these samples.  $\text{NaBH}_4$  may reduce  $\text{Ti}^{4+}$  to generated  $\text{Ti}^{3+}$  on the surface of  $\text{TiO}_2$  [14], in addition to reduce the metal precursors. The Cu  $2p_{3/2}$  and Ni  $2p_{3/2}$  peaks located at 932.5 eV and 855.5 eV can be detected on the metal loaded samples, which are assigned to  $\text{Cu}^0$  and  $\text{Ni}^0$  particles [31]. With gradual increase of Cu and

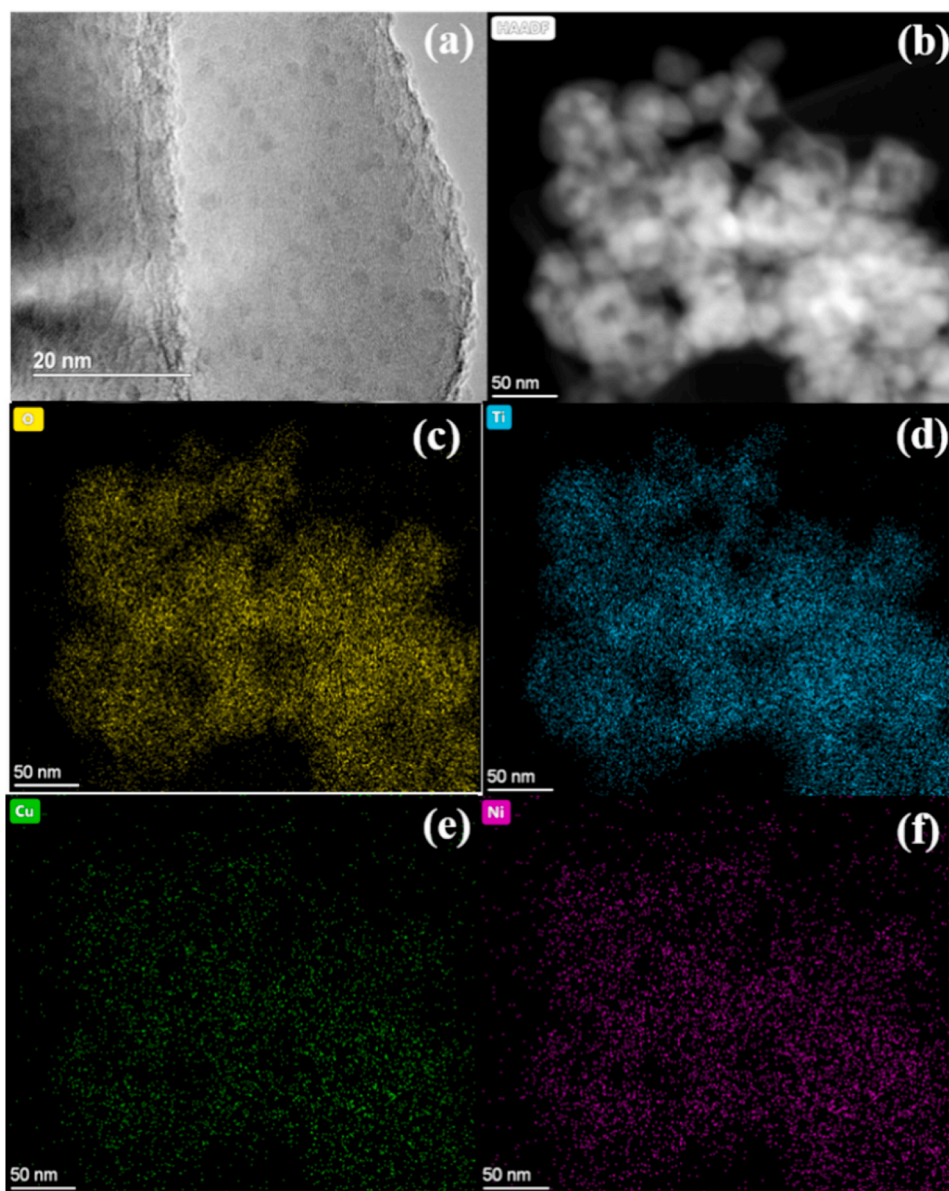


**Fig. 1.** (a) HR-TEM image of  $\text{Cu}_{0.5}\text{Ni}_{0.5}$ - $\text{TiO}_2$  sample; (b) HADDF image of  $\text{Cu}_{0.5}\text{Ni}_{0.5}$ - $\text{TiO}_2$  sample; (c) O elements mapping; (d) Ti element mapping; (e) Cu mapping; (f) Ni mapping.

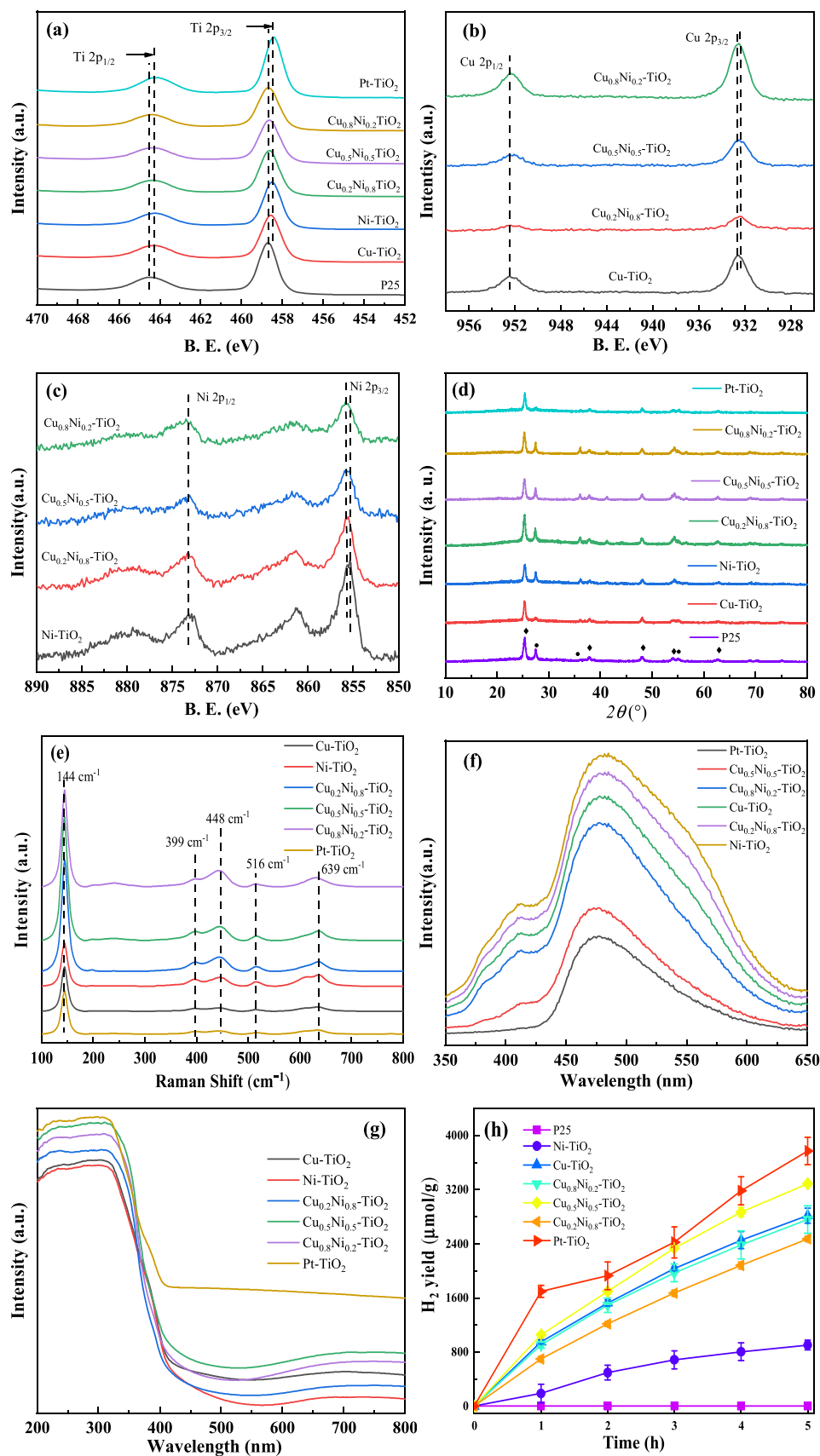


**Fig. 2.** Physicochemical characterizations of different  $\text{TiO}_2$  samples: (a–c) XPS spectra of Ti, Cu and Ni elements; (d) XRD patterns; (e) Raman spectra; (f) Photoluminescence spectra; (g) UV–visible spectra; (h) photocatalytic  $\text{H}_2$  production with glucose as sacrificial agent.



Ni loading mass, the XPS peak intensities of Cu and Ni elements were slightly increased.

The XRD patterns of the prepared samples confirm the anatase and rutile mixed phase structure of P25 (Fig. 2d). The peaks of crystallized metal phase can not be clearly observed due to their low contents. It is clearly shown that the peaks of rutile phase ( $27.5^\circ$ ) in Cu–TiO<sub>2</sub> and Pt–TiO<sub>2</sub> are much lower than the other samples, probably because the reduced metal particles prefer depositing on rutile phase sites so as to reduce the diffraction intensities. Then, we used Raman spectroscopy to further examine the chemical composition of surface modified TiO<sub>2</sub>. The strong Raman scattering bands at  $144\text{ cm}^{-1}$ ,  $399\text{ cm}^{-1}$ ,  $516\text{ cm}^{-1}$ , and  $639\text{ cm}^{-1}$  were observed (Fig. 2e), which are assigned to the anatase phase, and they can be attributed to the four Raman-active modes of anatase phase with the symmetries of  $E_g$ ,  $B_{1g}$ ,  $A_{1g}$ , and  $E_g$ , respectively. Another scattering band at  $448\text{ cm}^{-1}$  is assigned to rutile phase with symmetry of  $E_g$ . The scattering bands of  $293\text{ cm}^{-1}$  and  $540\text{ cm}^{-1}$  of CuO and NiO were not observed [36], implying the deposited Cu and Ni species were mainly composed by metal nanoparticles, rather than metal oxide nanoparticles. The Raman characterization along with the XPS and XRD characterization results demonstrate that the Cu and Ni nanoparticles were successfully deposited onto TiO<sub>2</sub> nanoparticles.

The charge carrier excitation and transfer properties of different Cu and Ni deposited TiO<sub>2</sub> samples in comparison with Pt–TiO<sub>2</sub> under light excitation were evaluated by photoluminescence (PL) spectroscopy (Fig. 2f). Under excitation by photons at 320 nm, the broad steady-state PL peaks of modified TiO<sub>2</sub> samples located around 440–550 nm, another small peak centered at 410 nm for the Cu and Ni modified sample, which could be resulted from the surface trap states of  $\text{Ti}^{3+}$  created by the  $\text{NaBH}_4$  reduction [14]. In general, the Cu/Ni co-deposited TiO<sub>2</sub> samples present lower PL peaks compared to the single metal deposited TiO<sub>2</sub>, indicating the charge-carrier recombination was effectively inhibited in the Cu/Ni co-deposited TiO<sub>2</sub> samples. The intensities of PL peaks follow the order of  $\text{Ni-TiO}_2 > \text{Cu}_{0.2}\text{Ni}_{0.8}\text{TiO}_2 > \text{Cu-TiO}_2 > \text{Cu}_{0.8}\text{Ni}_{0.2}\text{TiO}_2 > \text{Cu}_{0.5}\text{Ni}_{0.5}\text{-TiO}_2 > \text{Pt-TiO}_2$ , implying that Pt–TiO<sub>2</sub> and  $\text{Cu}_{0.5}\text{Ni}_{0.5}\text{-TiO}_2$  samples have better charge carrier transfer properties.

UV–Vis DRS spectra of different TiO<sub>2</sub> samples shown in Fig. 1e imply that the basic bandgap structures of TiO<sub>2</sub> are well preserved for all the samples and there are some band tail absorption peaks at wavelength of 400–500 nm for the transitional metals deposited TiO<sub>2</sub> samples in comparison with Pt–TiO<sub>2</sub>. This could be originated from the defect sites of  $\text{Ti}^{3+}$  created by  $\text{NaBH}_4$  reduction as observed from the PL analysis. In addition, the broad peaks centered at about 700 nm for the transitional metals deposited TiO<sub>2</sub> samples could be due to the surface plasma resonance effect of deposited Cu and Ni nanoparticles [37].

The photocatalytic H<sub>2</sub> generation performance of different TiO<sub>2</sub> samples was evaluated by adding glucose as a sacrificial agent under UV–visible light irradiation in a vacuum online analysis system. As shown in Fig. 1f, all the metals deposited TiO<sub>2</sub> samples can generate H<sub>2</sub> from water, whereas pure P25 sample can't generate H<sub>2</sub> at all. The H<sub>2</sub> evolution activities of different TiO<sub>2</sub> samples follow the trend of  $\text{Pt-TiO}_2 > \text{Cu}_{0.5}\text{Ni}_{0.5}\text{-TiO}_2 > \text{Cu-TiO}_2 = \text{Cu}_{0.8}\text{Ni}_{0.2}\text{-TiO}_2 > \text{Cu}_{0.2}\text{Ni}_{0.8}\text{-TiO}_2 > \text{Ni-TiO}_2$ . The H<sub>2</sub> evolution performance is basically consistent with the PL results. The H<sub>2</sub> yield of Cu–TiO<sub>2</sub> was about 3.2 times higher than that of Ni–TiO<sub>2</sub>, indicating Cu is more suitable as a H<sub>2</sub> evolution co-catalyst compared to Ni. The synergistic effect of Cu and Ni as co-catalysts can be observed from the results. The work functions of Cu and Ni are about 4.65 eV and 5.15 eV, respectively, which are higher than that of TiO<sub>2</sub> (4.2 eV) [31]. The injection of photo-generated electrons from TiO<sub>2</sub> conduction band into Cu or Ni metals can effectively inhibited electron-hole recombination. It was reported that the synergistic effect lies in the electron transfer from Ni to Cu on the dual Ni and Cu metals modified TiO<sub>2</sub> photocatalyst [31], which would lead to more efficient separation of photogenerated electron-hole pair. Therefore, the formation of Cu and Ni alloy or heterojunction is important for the synergistic H<sub>2</sub> production, which could be

the reason that the  $\text{Cu}_{0.5}\text{Ni}_{0.5}\text{-TiO}_2$  co-catalyst is the best than the other compositions. Surprisingly, due to the synergistic effect of dual metal deposition, the low-cost  $\text{Cu}_{0.5}\text{Ni}_{0.5}\text{TiO}_2$  photocatalyst exhibited comparable H<sub>2</sub> evolution activity with the benchmark Pt–TiO<sub>2</sub> photocatalyst.

### 3.2. Enzymatic hydrolysis of cellulose

The enzymatic hydrolysis of cellulose was investigated by varying the experimental parameters to screen out the best cellulose conversion condition (Fig. 3). Firstly, the mass ratio of enzyme/cellulose was studied with changing the ratio from 1:12.5–1:100 (Fig. 3a). Generally, the maximum glucose yield was obtained with the mass ratio of 1:25. Then, the temperature effect on cellulose hydrolysis was studied by varying reaction temperature from 40 °C to 60 °C with cellulase (from *Trichoderma reesei*) (Fig. 3b). The enzymatic activity was quite sensitive to the hydrolysis temperature, and the maximum glucose yield (about 0.55 g/L) was obtained at 45 °C with cellulose conversion efficiency of 26.8 %. Subsequently, another four types of commercial cellulase obtained from different sources were picked out to compare the cellulase activity at 45 °C (Fig. 3c). The cellulase from *Trichoderma reesei* exhibits the best activity among the five types of cellulase. Furthermore, the solution pH plays important role in cellulose conversion, and the best solution pH was found to be pH 5.5 (Fig. 3d). The glucose yield reached to 1.15 g/L, and cellulose conversion ratio reached to about 56 % after 48 h reaction.

The inorganic salts in solution may influence the enzymatic activity as well, so their effects on the glucose yields were studied by adding eight kinds of inorganic salts with different concentrations into the cellulose/cellulase suspension. As shown in Fig. 3e, the univalent  $\text{K}^+$  and  $\text{Na}^+$  present the most distinguished promotion effects, while the activity enhancement by divalent  $\text{Mg}^{2+}$ ,  $\text{Ca}^{2+}$ ,  $\text{Cu}^{2+}$  and  $\text{Zn}^{2+}$  and trivalent  $\text{Fe}^{3+}$  and  $\text{Sm}^{3+}$  ions are not remarkable. It was found out the maximum glucose yield was obtained in the presence of 0.03 M  $\text{K}^+$ , which exhibits about 80 % enhancement of glucose yield. The reasons accounting for the different roles of inorganic salts on the enzymatic activity were further investigated. Since the cellulase is mainly composed by endoglucanase (EG enzyme), exoglucanase (CBH enzyme) and glucosidase ( $\beta$ –G enzyme). Each enzymatic activity was tested with three different substrates including methylcellulose, microcrystalline cellulose, and D–salicylate for EG enzyme, CBH enzyme and  $\beta$ –G enzyme, respectively. The hydrolysis condition was the same with that of cellulose hydrolysis. As shown in Figs. S1–4, the effect of monovalent  $\text{Na}^+$  and  $\text{K}^+$  concentrations on substrate conversion is similar for the  $\beta$ –G enzyme and cellulase, and they have strong enhancement effect on  $\beta$ –G enzyme activity, which mainly plays the function of conversion of cellulose into glucose. On the other hand, divalent metal ions generally promote the EG enzyme activity, except that  $\text{Cu}^{2+}$  basically inhibits the enzyme activities. Trivalent  $\text{Fe}^{3+}$  and  $\text{Sm}^{3+}$  can promote CBH enzyme activity.

### 3.3. Combined enzymatic catalysis and photocatalysis

According to the proposed reaction mechanism, the enzyme catalysis module and photocatalysis module should be connected with a membrane which allows glucose migration and blocks oxidative species migration between the two reactor modules. Firstly, we tested six types of membranes with different compositions and pore sizes for measuring glucose permeability under static condition by dropping 5.5 mM of glucose into the inner reactor module and monitoring the glucose concentration in outer reactor module at different time intervals. The glucose may transfer across the membrane driven by concentration gradient between the two modules. The results indicate that glass fiber membrane with 0.45  $\mu\text{m}$  pore size has the best glucose permeability among the tested membranes (Fig. 4a), implying that the membrane material composition is the key factor influencing the glucose

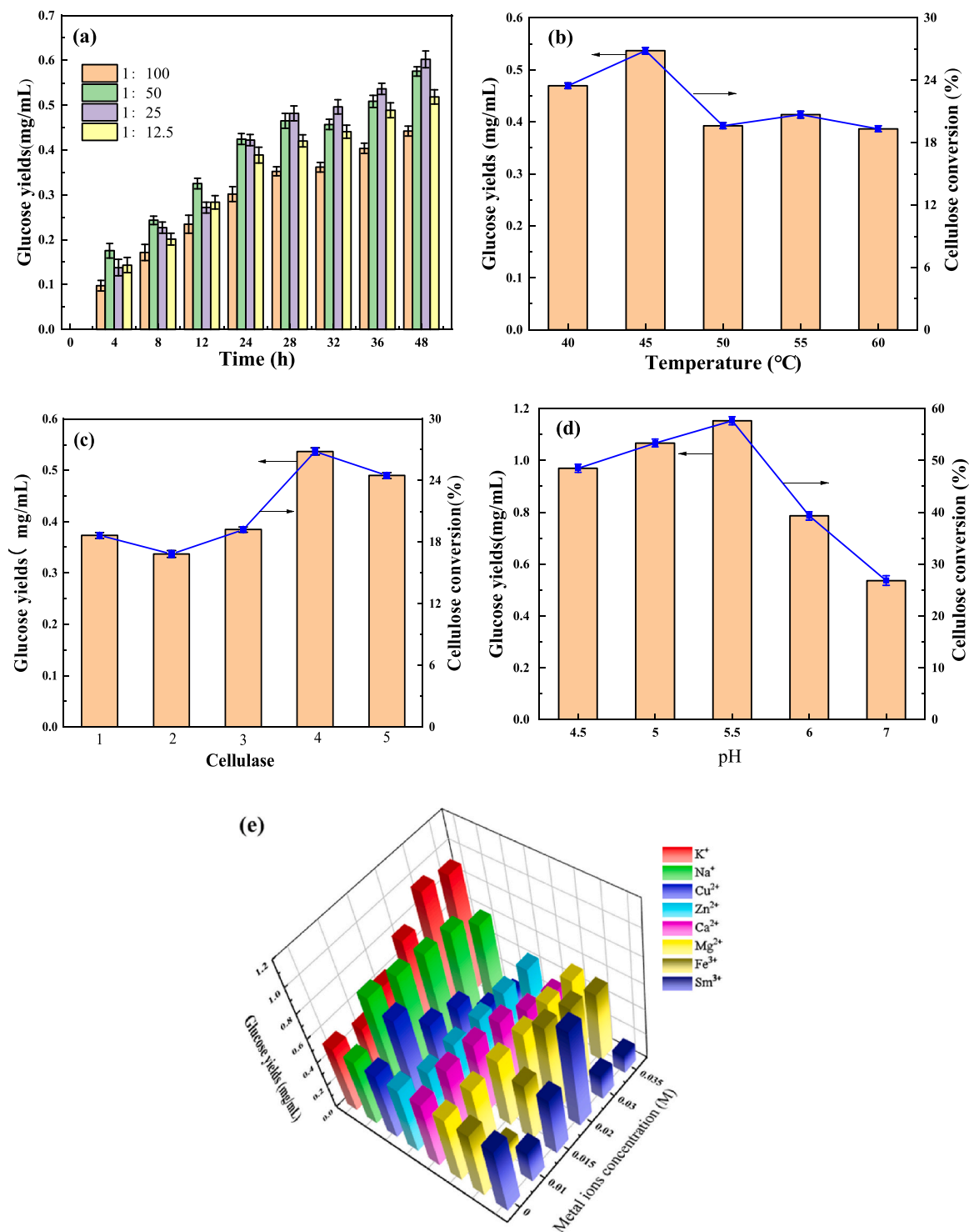


**Fig. 3.** Different experimental parameters on the glucose production from cellulose hydrolysis: (a) effect of mass ratio of enzyme/cellulose; (b) effect of temperature; (c) effect of types of cellulases (1: from *Aspergillus niger* (carrier for starch), 2: from *Trichoderma Viride*, food grade) 3: from *Trichoderma Viride*, 4: from *Trichoderma reesei*, 5: from *Aspergillus niger* (carrier for dextrin)); (d) effect of pH on the glucose production; (e) effect of types and concentrations of metal ions.

permeation. After 24 h, the glucose concentration in two modules nearly reached to theoretical equilibrium condition. Then, the blockage of hydroxyl radical as the main oxidant generated by photocatalysis passing through the membrane was also evaluated. It is generally thought that the diffusion length of  $\bullet\text{OH}$  ranged about few  $\mu\text{m}$  and the lifetime of

$\bullet\text{OH}$  is quite short [38], and the thickness of inorganic membrane is about 500  $\mu\text{m}$ , therefore, it is hard for  $\bullet\text{OH}$  radical crossing over the membrane. Most of them may recombine with each other. The in situ generated  $\bullet\text{OH}$  by photocatalysis on  $\text{Cu}_{0.5}\text{Ni}_{0.5}\text{TiO}_2$  catalyst was evaluated by using terephthalic acid probe according to the fluorescence

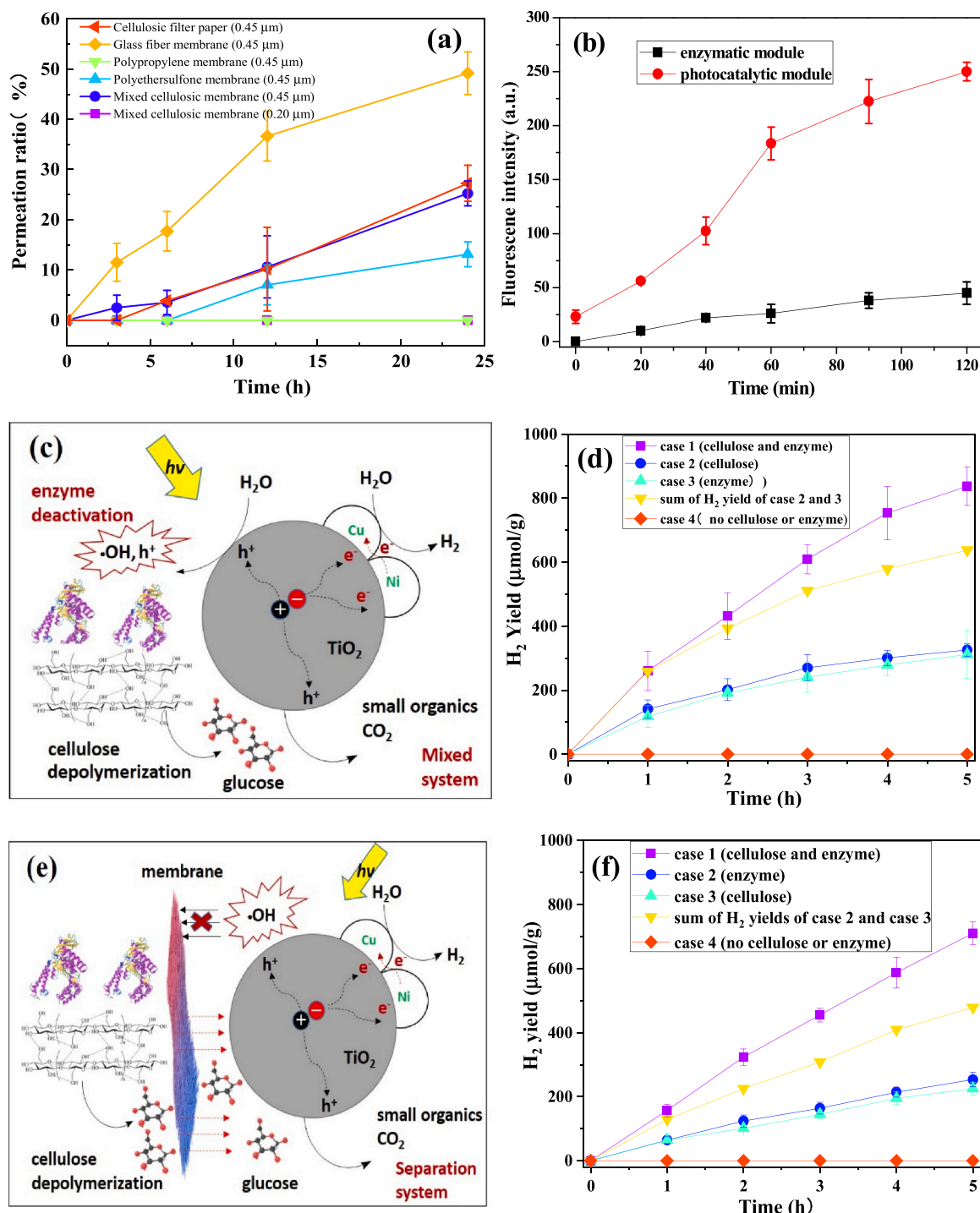


**Fig. 4.** (a) Glucose permeation capabilities of different membranes; (b) hydroxyl radical quantification in different modules based on fluorescence intensity signals; (c) proposed photocatalytic H<sub>2</sub> generation mechanism in mixed system; (d) photocatalytic H<sub>2</sub> generation at different conditions in mixed system; (e) proposed photocatalytic H<sub>2</sub> generation mechanism in membrane-separation system; (f) photocatalytic H<sub>2</sub> generation at different conditions in membrane-separation system.

intensity signals. As shown in Fig. 4b, the relative fluorescence intensity signals at 425 nm in the photocatalytic module were significantly higher than that in the enzymatic module, indicating that the membrane can efficiently block the migration of  $\bullet\text{OH}$  from photocatalytic module into the enzymatic module.

Then, the photocatalytic H<sub>2</sub> production by coupling enzyme catalytic hydrolysis of cellulose with the Cu<sub>0.5</sub>Ni<sub>0.5</sub>-TiO<sub>2</sub> photocatalyst was performed in both all-in-one mixed and membrane-separated systems as shown in Fig. 4c–f. In the case of mixed system, when the Cu<sub>0.5</sub>Ni<sub>0.5</sub>

-TiO<sub>2</sub> photocatalyst, cellulose powder and cellulase were all suspended in a one single reactor (Fig. 4c), the H<sub>2</sub> could be efficiently generated as shown in Fig. 4d. However, if the cellulase and cellulose were not simultaneously present in the reactor, the H<sub>2</sub> yields were remarkably reduced. There are some soluble organic components from the enzyme and cellulose could be served as sacrificial agents for improving photocatalytic H<sub>2</sub> production, in comparison with the control test. Even the cellulose power was firstly treated by water washing to remove possible soluble fragments, the solid cellulose could be played as a sacrificial

agent as well, as there are many reports on direct photoreforming of cellulose for  $H_2$  production [8,24]. It should be noted that,  $K^+$  has little role on the  $H_2$  production. On the other hand, one can conclude that the synergistic effect between photocatalysis and enzymatic hydrolysis was shown according to the  $H_2$  yields, when the cellulose and enzyme were present in the mixed system. The  $H_2$  yield in the mixed system is larger than the sum of  $H_2$  yields in case 2 and case 3. The enhanced  $H_2$  yield was due to the in situ generated carbohydrates (e.g. glucose) from cellulose hydrolysis which played the role as efficient hole scavengers.

In the membrane-separation system shown in Fig. 4e, the photocatalytic reactor module and enzymatic reactor module was separated with the glass fiber membrane, which would allow the enzymatic hydrolysis and photocatalysis to proceed separately and therefore inhibit the attack of enzyme by the oxidants generated by photocatalysis. The control experiments indicated that without adding cellulose powder or enzyme into the enzymatic reactor module, there was no  $H_2$  evolved from the photocatalytic module in the presence of photocatalyst (Fig. 4f). After loading cellulose or enzyme into the enzymatic module, the  $H_2$  evolution was markedly enhanced, because the soluble organic components within cellulose or enzyme could permeate across membrane into photocatalytic module part. However, the  $H_2$  production was significantly enhanced if both cellulose and enzyme were loaded into the enzyme module due to the synergistic effect. In this case, simultaneous enzymatic depolymerization of cellulose to generate glucose and the sacrificial photocatalytic  $H_2$  production took place within each module. The generated glucose passed through the membrane and assisted the photocatalytic generation of  $H_2$  from water splitting.

The advantage of membrane-separation system and synergistic effect in  $H_2$  production were more prominent in the long-time (24 h) running experiment as shown in Fig. 5a. In the initial 6 h reaction, the  $H_2$  yield in the mixed system was much higher than that in the membrane-separation system, however the  $H_2$  yield in the membrane-separation system gradually exceeded the  $H_2$  yield in the mixed system. The  $H_2$  yields in 5 h and 24 h under UV-visible light irradiation reached to about  $710.2 \mu\text{mol/g.cat}$  and  $1948.7 \mu\text{mol/g.cat}$ , respectively, and presented  $H_2$  production efficiencies of  $142.2 \mu\text{mol/h}\cdot\text{g.cat}$  (5 h) and  $81.1 \mu\text{mol/h}\cdot\text{g.cat}$  (24 h). Under the optimized condition, the apparent quantum efficiency (AQE<sub>5</sub>) for  $H_2$  production in the initial 5 h ( $36.51 \mu\text{mol}$ ) under  $365 \pm 10 \text{ nm}$  irradiation was about 3.07 % according to the calculation as shown below.

$$N_p = E/hc = (43.24 \times 10^{-3} \times 3600 \times 5 \times 365 \times 10^{-9}) / (6.626 \times 10^{-34} \times 3 \times 10^8) = 1.43 \times 10^{21}$$

$$\text{AQE} = N_p / N_p \times 100 \% = (2 \times 6.02 \times 10^{23} \times 36.51 \times 10^{-6}) / (1.43 \times 10^{21} \times 100) \% = 3.07 \%$$

The  $H_2$  production in the mixed system was nearly ceased after 8 h reaction, probably because the deactivation of enzyme by the photocatalytic oxidation so that the enzymatic hydrolysis of cellulose was completely inhibited after 8 h reaction. In contrast, the damage of enzyme could be prevented by the physical membrane separation. The  $H_2$  production in the separation system was remained about 24 h with gradually reduced  $H_2$  evolution rate, probably due to the depletion of organic carbohydrates in the photocatalytic module. To demonstrate the

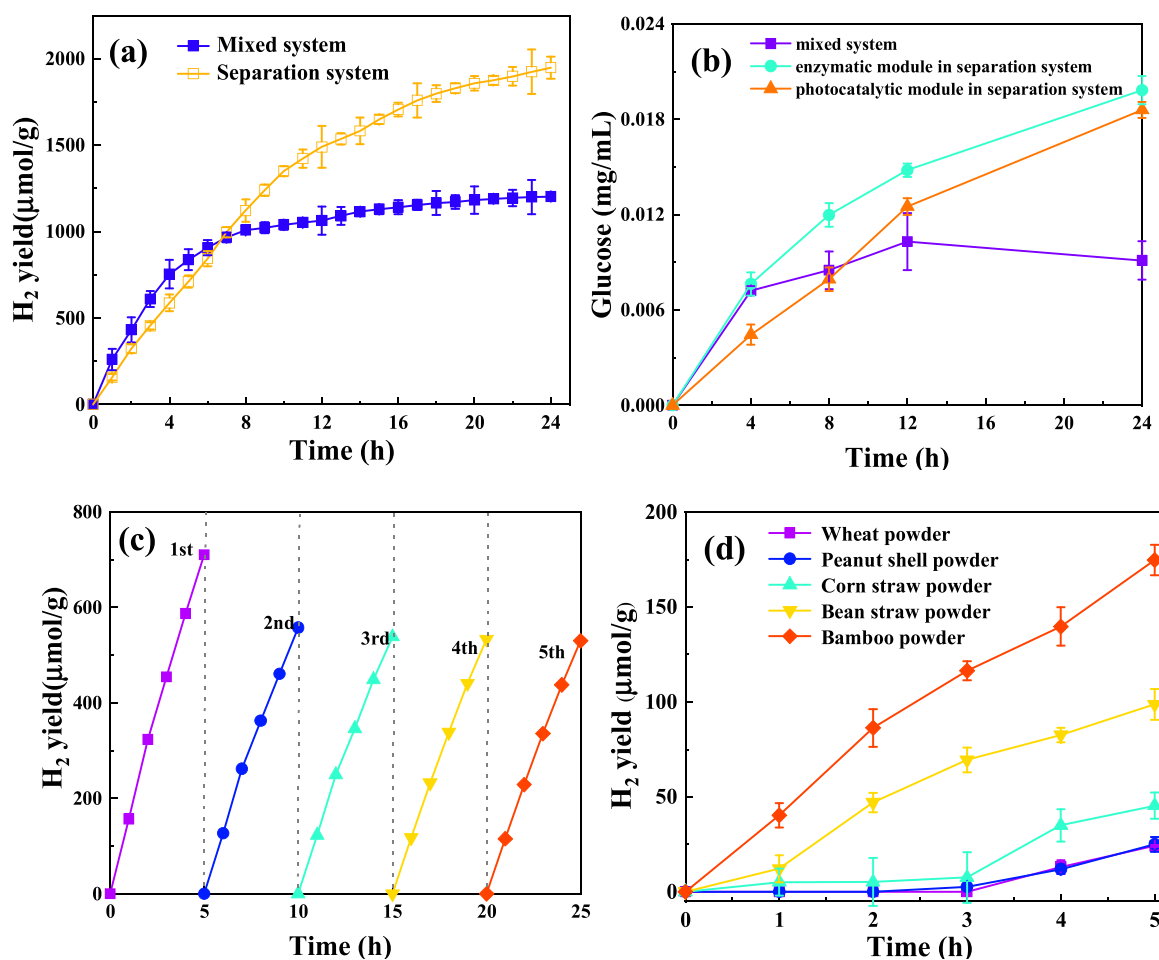


Fig. 5. (a) Comparison of  $H_2$  production in the mixed and membrane-separation systems during 24 h; (b) glucose concentration in the mixed and membrane-separation systems; (c) repeated photocatalytic  $H_2$  production utilizing recycled  $\text{Cu}_{0.5}\text{Ni}_{0.5}-\text{TiO}_2$  photocatalyst in the membrane-separation system; (d) photocatalytic  $H_2$  production utilizing raw biomass substances in the membrane-separation system.



reasons for the decay in photocatalytic H<sub>2</sub> evolution rate, we additionally fed more cellulose powder into the enzymatic module after 24 h reaction. The H<sub>2</sub> evolution rate was slightly improved again. It seems that the enzymatic activity of cellulase was significantly reduced after 24 h reaction. There are many factors influencing the enzymatic activity of cellulase, such as temperature, pH, substrate concentration, inhibitor, competitive adsorption, etc. Therefore, it is necessary to regulate both the two individual processes to exert their advantages and functions.

To demonstrate the roles of membrane in passing glucose between the two modules, the glucose concentration in each reaction system was monitored during H<sub>2</sub> production process (Fig. 5b). In the mixed system, the glucose concentration gradually increased in the first 12 h and then slightly decreased with further reaction. The enzymatic decomposition of cellulose was inhibited during the long-time reaction, whereas the generated glucose could be further oxidized by the photocatalysis so that the glucose concentration was reduced in the mixed system. In the separation system, the glucose concentration in each module was continuously increased during the 24 h reaction, and its concentration in photocatalytic module was slightly lower than that in the enzymatic module, which reflects the role of membrane in transferring glucose and preventing photocatalytic oxidation of enzyme. However, the glucose concentration in each case (0.006–0.02 mg/L) was significantly lower than the theoretical produced contents from enzymatic hydrolysis, indicating that most hydrolyzed glucose was oxidized by photocatalysis in the H<sub>2</sub> production process. These results confirm the advantage of membrane–separation system in converting biomass for H<sub>2</sub> production.

The effect of photocatalyst concentration in the separation system was further studied (Fig. S5), and the optimum concentration of Cu<sub>0.5</sub>Ni<sub>0.5</sub>–TiO<sub>2</sub> was 1.0 g/L. Further increasing the photocatalyst concentration to 1.25 g/L did not enhance the H<sub>2</sub> production yield due to the light–blocking and particle agglomeration effects. As shown in Fig. S6, the effect of light intensity on the H<sub>2</sub> production was investigated, and the results show that the maximum H<sub>2</sub> production was realized with the light intensity of 900–1000 mW/cm<sup>2</sup>. The Cu<sub>0.5</sub>Ni<sub>0.5</sub>–TiO<sub>2</sub> was stable in terms of producing H<sub>2</sub> during the five repeated experiments employing the recycled Cu<sub>0.5</sub>Ni<sub>0.5</sub>–TiO<sub>2</sub> photocatalyst as shown in Fig. 5c. The H<sub>2</sub> production from raw biomass materials is a more ideal approach for biomass conversion, and the activities were tested as shown in Fig. 5d. The H<sub>2</sub> yields from different biomass materials follows the order of bamboo > soybean straw > corn straw > peanut shell = wheat straw. The H<sub>2</sub> yield from the bamboo powder was the highest, but was lower than that produced in the presence of same mass of cellulose powder. The lignin and semicellulose parts on the biomass materials prevent the enzymatic hydrolysis of cellulose, so as to reduce the H<sub>2</sub> production yields.

#### 4. Conclusions

In summary, this work demonstrated that enzymatic hydrolysis of cellulosic biomass and photocatalytic H<sub>2</sub> production processes can be integrated via an inorganic membrane for biomass to H<sub>2</sub> production. Through a facile NaBH<sub>4</sub> reduction approach, the same ratio of Cu and Ni nanoparticles were deposited on TiO<sub>2</sub>, which exhibited the superior photocatalytic H<sub>2</sub> generation performance even comparable to Pt–TiO<sub>2</sub>. The synergistic effect of Cu and Ni co–deposition was attributed to the electron transfer from Ni to Cu, which benefits for the photogenerated charge carrier separation and H<sub>2</sub> production. In addition, the optimum cellulose hydrolysis condition was found out with mass ratio of cellulase (from *Trichoderma reesei*)/cellulose as 1: 25, and the glucose yield reached to over 1.15 g/L in 32 h at condition of pH 5.5 and 45 °C in the presence of 0.03 M K<sup>+</sup>. It was found out the activation of β–G enzyme in cellulase by K<sup>+</sup> mainly enhanced the glucose yield. Upon the utilization of glass fiber membrane for interconnecting enzymatic hydrolysis module and photocatalytic module, the photocatalytic H<sub>2</sub> production performance was significantly enhanced compared to that without membrane separation, because the membrane can not only allow

glucose to transfer from enzymatic module to photocatalytic module, but also block the oxidative radical reverse transfer in order to prevent inactivation of enzyme. The apparent quantum efficiency under 365 ± 10 nm irradiation in initial 5 h was about 3.07 %. Based on this strategy, environmental–friendly cellulosic biomass conversion to H<sub>2</sub> could be further developed by integrating microbial process and photocatalytic process.

#### CRedit authorship contribution statement

**Zhaoyi Li:** Investigation, analysis. **Zhen Sun:** Investigation. **Guan Zhang:** Writing, Funding acquisition, Project administration.

#### Declaration of Competing Interest

The authors declare that they have no known competing financial interests or personal relationships that could have appeared to influence the work reported in this paper.

#### Data availability

Data will be made available on request.

#### Acknowledgements

This work was supported by Shenzhen Science and Technology Innovation Commission, China (No. JCYJ20210316074858001), State Key Laboratory of Urban Water Resource and Environment, China (Harbin Institute of Technology, No. 2021TS20).

#### Appendix A. Supporting information

Supplementary data associated with this article can be found in the online version at doi:10.1016/j.apcatb.2023.123069.

#### References

- [1] M. Eibinger, J. Sattelkow, T. Ganner, H. Plank, B. Nidetzky, Single-molecule study of oxidative enzymatic deconstruction of cellulose, *Nat. Commun.* 8 (2017) 894.
- [2] C. Chen, L. Dai, L. Ma, R. Guo, Enzymatic degradation of plant biomass and synthetic polymers, *Nat. Chem. Rev.* 4 (2021) 114–126.
- [3] U. Bornscheuer, K. Buchholz, J. Seibel, Enzymatic degradation of (ligno)cellulose, *Angew. Chem. Int. Ed.* 53 (2014) 10876–10893.
- [4] R. Zhang, Z. Hu, H. Peng, P. Liu, Y. Wang, J. Li, J. Lu, Y. Wang, T. Xia, L. Peng, High density cellulose nanofibril assembly leads to upgraded enzymatic and chemical catalysis of fermentable sugars, cellulose nanocrystals and cellulase production by precisely engineering cellulose synthase complexes, *Green. Chem.* 25 (2023) 1096–1106.
- [5] H. Lu, S. Liu, Y. Shi, Q. Chen, Efficient delignification of sugarcane bagasse by Fenton oxidation coupled with ultrasound–assisted NaOH for biotransformation from *Agaricus sinodeliciosus* var. Chaidam, *Chem. Eng. J.* 448 (2022), 137719.
- [6] B. Bissaro, E. Kommedal, A.K. Rohr, V.G.H. Eijsink, Controlled depolymerization of cellulose by light–driven lytic polysaccharide oxygenases, *Nat. Commun.* 11 (2020) 890.
- [7] J. Zou, G. Zhang, X. Xu, One pot photoreforming of cellulosic biomass waste to hydrogen by merging photocatalysis with acid hydrolysis, *Appl. Catal. A* 563 (2018) 73–79.
- [8] G. Zhang, C. Ni, X. Huang, A. Welgamage, L.A. Lawton, P.K.J. Robertson, J.T. S. Irvine, Simultaneous cellulose conversion and hydrogen production assisted by cellulose decomposition under UV–light photocatalysis, *Chem. Commun.* 52 (2016) 1673.
- [9] Z. Li, S. Qu, G. Zhang, Photocatalytic H<sub>2</sub> production from water splitting employing depolymerized cellulose through LiCl activation as sacrificial agent, *Int. J. Hydrogen Energy* 48 (2023) 9647–9658.
- [10] Z.C. Litman, Y. Wang, H. Zhao, J.F. Hartwig, Cooperative asymmetric reactions combining photocatalysis and enzymatic catalysis, *Nature* 560 (2018) 355–359.
- [11] Z. Sun, J. Wang, S. Lu, G. Zhang, Integrating enzymatic biomass hydrolysis with photocatalysis for cocatalyst free H<sub>2</sub> production from water on porous carbon doped brookite–anatase heterophase titania, *Renew. Energy* 197 (2022) 151–160.
- [12] W. Zhang, E. Fernandez–Fueyo, Y. Ni, M. van Schie, J. Gacs, R. Renirie, R. Wever, F.G. Mutti, D. Rother, M. Alcalde, F. Hollmann, Selective aerobic oxidation reactions using a combination of photocatalytic water oxidation and enzymatic oxyfunctionalizations, *Nat. Catal.* 1 (2018) 55–62.
- [13] E. Huang, G. Liu, G. Zhang, X. Xu, In situ fabrication of two–dimensional g–C<sub>3</sub>N<sub>4</sub>/Ba<sub>5</sub>Ta<sub>4</sub>O<sub>15</sub> nanosheet heterostructures with efficient charge separations and

- photocatalytic hydrogen evolution under visible light illumination, *Dalton Trans.* 47 (2018) 4360–4367.
- [14] G. Zhang, J. Zou, X. Xu, Reduced 3d transition metal oxides work as solid–state sources of solvated electrons and directly inject electrons into water for H<sub>2</sub> production under mild thermal or IR excitation, *Adv. Sustain. Syst.* 2 (2018), 1700139.
  - [15] J. Hui, G. Zhang, C. Ni, J. Irvine, Promoting photocatalytic H<sub>2</sub> evolution by tuning cation deficiency in La and Cr co–doped SrTiO<sub>3</sub>, *Chem. Commun.* 53 (2017) 10038–10042.
  - [16] T. Hisatomi, K. Domen, Reaction systems for solar hydrogen production via water splitting with particulate semiconductor, *Nat. Catal.* 2 (2019) 387–399.
  - [17] T. Takata, J. Jiang, Y. Sakata, M. Nakabayashi, N. Shibata, V. Nandal, K. Seki, T. Hisatomi, K. Domen, Photocatalytic water splitting with a quantum efficiency of almost unity, *Nature* 581 (2020) 411–414.
  - [18] H. Nishiyama, T. Yamada, M. Nakabayashi, Y. Maehara, M. Yamaguchi, Y. Kuromiya, Y. Nagatsuma, H. Tokudome, S. Akiyama, T. Watanabe, R. Narushima, S. Okunaka, N. Shibata, T. Takata, T. Hisatomi, K. Domen, Photocatalytic solar hydrogen production from water on a 100–m<sup>2</sup> scale, *Nature* 598 (2021) 304–307.
  - [19] C. Li, J. Liu, H. Li, K. Wu, J. Wang, Q. Yang, Covalent organic frameworks with high quantum efficiency in sacrificial photocatalytic hydrogen evolution, *Nat. Commun.* 13 (2022) 2357.
  - [20] X. Yang, J. Cui, X. Liu, Q. Zhang, D. Wang, J. Ye, L. Liu, Boosting photocatalytic overall water splitting over single–layer graphene coated metal cocatalyst, *Appl. Catal. B: Environ.* 325 (2023), 122369.
  - [21] T. Zhang, S. Lu, Sacrificial agents for photocatalytic hydrogen production: effects, cost, and development, *Chem. Catal.* 2 (2022) 1502–1505.
  - [22] P. Tao, X. Wang, Q. Zhao, H. Guo, L. Liu, X. Qi, W. Cui, Framework Ti–rich titanium silicalite–1 zeolite nanoplates for enhanced photocatalytic H<sub>2</sub> production from CH<sub>3</sub>OH, *Appl. Catal. B: Environ.* 325 (2023), 122392.
  - [23] L. Zhang, W. Wang, S. Zeng, Y. Su, H. Hao, Enhanced H<sub>2</sub> evolution from photocatalytic cellulose conversion based on graphitic carbon layers on TiO<sub>2</sub>/NiO<sub>x</sub>, *Green. Chem.* 20 (2018), 3008–2013.
  - [24] M.F. Kuehnel, E. Reisner, Solar hydrogen generation from lignocellulose, *Angew. Chem. Int. Ed.* 57 (2018) 3290.
  - [25] V.C. Nguyen, N.J. Ke, L.D. Nam, B.S. Nguyen, Y.K. Xiao, Y.L. Lee, H. Teng, Photocatalytic reforming of sugar and glucose into H<sub>2</sub> over functionalized graphene dots, *J. Mater. Chem. A* 7 (2019) 8384–8393.
  - [26] G. Zhang, G. Kim, W. Choi, Visible light driven photocatalysis mediated via ligand–to–metal charge transfer (LMCT): an alternative approach to solar activation of titania, *Energy Environ. Sci.* 7 (2014) 954–966.
  - [27] G. Zhang, C. Kim, W. Choi, Poly(4–vinylphenol) as a new stable and metal–free sensitizer of titania for visible light photocatalysis through ligand–to–metal charge transfer process, *Catal. Today* 281 (2017) 109–116.
  - [28] A.K. Rathi, H. Kmentova, A. Naldoni, A. Goswami, M.B. Gawande, R.S. Varma, S. Kment, R. Zboril, Significant enhancement of photoactivity in hybrid TiO<sub>2</sub>/g–C<sub>3</sub>N<sub>4</sub> nanorod catalysts modified with Cu–Ni–based nanostructures, *ACS Appl. Nano Mater.* 1 (2018) 2526–2535.
  - [29] H. Tian, S. Kang, X. Li, L. Qin, M. Ji, J. Mu, Fabrication of an efficient noble metal–free TiO<sub>2</sub>–based photocatalytic system using Cu–Ni bimetallic deposit as an active center of H<sub>2</sub> evolution from water, *Sol. Energy Mater. Sol. Cells* 134 (2015) 309–317.
  - [30] S. Zhu, X. Xie, S. Chen, S. Tong, G. Lu, D. Pui, J. Sun, Cu–Ni nanowire–based TiO<sub>2</sub> hybrid for the dynamic photodegradation of acetaldehyde gas pollutant under visible light, *Appl. Surf. Sci.* 408 (2017) 117–124.
  - [31] D. Spanu, A. Minguzzi, S. Recchia, F. Shahvardanfard, O. Tomanec, R. Zboril, P. Schmuki, P. Ghigna, M. Altomare, An operando X–ray absorption spectroscopy study of a NiCu–TiO<sub>2</sub> photocatalyst for H<sub>2</sub> evolution, *ACS Catal.* 10 (2020) 8293–8302.
  - [32] M. Wang, P. Wang, H. Long, X. Wang, F. Chen, H. Yu, Improved H–adsorption ability of Cu in CuNi alloy nanodots toward the efficient photocatalytic H<sub>2</sub>–evolution activity of TiO<sub>2</sub>, *Dalton Trans.* 51 (2022) 14526.
  - [33] M. Cheng, T. Shi, H. Guan, S. Wang, X. Wang, Z. Jiang, Clean production of glucose from polysaccharides using a micellar heteropolyacid as a heterogeneous catalyst, *Appl. Catal. B: Environ.* 107 (2011) 104–109.
  - [34] F. Liu, A. Zheng, I. Noshadi, F. Xiao, Design and synthesis of hydrophobic and stable mesoporous polymeric solid acid with ultra strong acid strength and excellent catalytic activities for biomass transformation, *Appl. Catal. B: Environ.* 136–137 (2013) 193–201.
  - [35] F. Deng, S. Li, Y. Cao, M.A. Fang, J. Qu, Z. Chen, S. Qiu, A dual–cathode pulsed current electro–Fenton system: Improvement for H<sub>2</sub>O<sub>2</sub> accumulation and Fe<sup>3+</sup> reduction, *J. Power Sources* 466 (2020), 228342.
  - [36] M. Francisco, V. Mastelaro, P. Nascente, A. Florentino, Activity and characterization by XPS, HR–TEM, Raman spectroscopy, and BET surface area of CuO/CeO<sub>2</sub>–TiO<sub>2</sub> catalyst, *J. Phys. Chem. B* 105 (2001) 10515–10522.
  - [37] M. Sayed, J. Yu, G. Liu, M. Jarniec, Non–noble plasmonic metal–based photocatalyst, *Chem. Rev.* 122 (2022) 10484–10537.
  - [38] W. Kim, T. Tachikawa, G. Moon, T. Majima, W. Choi, Molecular–level understanding of the photocatalytic activity difference between anatase and rutile nanoparticles, *Angew. Chem. Int. Ed.* 53 (2014) 14036–14041.